Article:

John, E.D.A. orcid.org/0000-0002-8707-4197, Boxall, J.B. orcid.org/0000-0002-4681-6895, Collins, R.P. orcid.org/0000-0001-5449-8535 et al. (2 more authors) (2026) Multiaxial notch fatigue of corroded cast iron pipes. International Journal of Fatigue, 202. 109247. ISSN: 0142-1123

https://doi.org/10.1016/j.ijfatigue.2025.109247

International Journal of Fatigue 202 (2026) 109247

Contents lists available at ScienceDirect

International Journal of Fatigue

journal homepage: www.elsevier.com/locate/ijfatigue

Multiaxial notch fatigue of corroded cast iron pipes

E.D.A. John [a], J.B. Boxall [a], R.P. Collins [a], E.T. Bowman [a], L. Susmel [b,*]

[a] School of Mechanical, Aerospace and Civil Engineering, Sir Frederick Mappin Building, The University of Sheffield, Mappin Street, Sheffield S1 4DT, UK
[b] School of Engineering and Built Environment, Sheffield Hallam University, Harmer Building, Sheffield S1 1WB, UK

ARTICLE INFO

Keywords:
Multiaxial
Notch
Cast iron
Pipe
Bending
High-cycle fatigue

ABSTRACT

Grey Cast Iron (GCI) water pipes often develop localised corrosion pits that act as notches and can also experience biaxial fatigue stresses, resulting in a multiaxial notch fatigue problem. This paper experimentally investigates for the first time, the high-cycle fatigue sensitivity of GCI to localised notches, under bending and biaxal loading, and validates a multiaxial notch fatigue model for GCI. The work uses a recently developed, novel biaxial fatigue experiment to generate the first fatigue data for GCI featuring pit-like notches. Approximately 40 new fatigue tests were completed to calibrate and test four multiaxial notch fatigue models, and to investigate the effects of notch root radius, localised notches, bending loading, and biaxial loading. The data shows that pit-like notches can have a statistically significant influence on the fatigue strength of GCI when $K_{t,n} > 4$. Additionally, 180° out-of-phase biaxial loading was found to reduce the fatigue strength of un-notched specimens by 28 %. The Effective Volume notch fatigue model, coupled with the linear-elastic Smith-Watson-Topper criterion, was found to give good predictions for notched GCI pipes subject to uniaxial and bending loading. This work highlights the ability of the Effective Volume approach to make good fatigue life estimates for thin, notched components featuring inclusions, where critical distance-based approaches performed less well. Future work on similar problems may wish to consider this approach.

1. Introduction

The UK water industry has committed to halving leakage rates by 2050, compared to 2017/18 levels, which will require targeted pipe replacement [1]. To decide which pipes to replace one must be able to assess the relative health of a given pipe. Grey Cast Iron (GCI) pipes are old, very common, and have high failure rates per km [2,3], making assessing the health of the remaining GCI pipes a priority. The damp, aerated conditions found in the soil surrounding many buried GCI water pipes promotes the growth of corrosion pitting on the external surface of the pipes [4]. The corrosion process replaces the original iron with a much weaker corrosion product [5,6], which is often modelled as a pit in the pipe wall for structural analysis [7,8]. As a result, corrosion pitting can act as a notch, concentrating stress in the pipe wall and causing cracks for form under loading that would not damage an un-corroded pipe [7].

Small diameter GCI water pipes are commonly found to have developed circumferential cracks, which are usually attributed to bending loads [2,3,9]. Many pipes are buried under roads, so a potential source of bending loads is vehicle loading [10]. The time variable nature of vehicle loading means small diameter pipes may develop leaking cracks due to bending fatigue loading. Water pipes are also often exposed to substantial fluctuations in internal water pressure [11,12]. No validated models are available that can predict the damaging effect of corrosion pitting on the fatigue strength of GCI pipes subject to bending loads, or combined bending and internal pressure loads [13,14]. This means asset managers are unable to accurately assess the damaging effect of corrosion pitting on the GCI pipes they are responsible for, impeding their ability to make asset health assessments.

GCI is often credited with very low fatigue notch sensitivity [15]. The available notch fatigue data for GCI is limited, covering only solid cylindrical specimens with sharp circumferential V-notches under uniaxial and rotating bending loads [16,17]. This data is limited in its relevance to corrosion pitting in GCI pipes where localised, blunt notches are common, and the material depth behind the notch may be a couple of mm or less [7]. Data quoted by Heywood [18] for several different GCIs give bending fatigue strengths 1.38 to 1.69 times higher than the axial fatigue strength. No data is available for bending fatigue of locally notched GCI.

To predict the fatigue strength of notched GCI, Heywood [18] proposed an empirical equation that predicts the fatigue strength reduction

---

* Corresponding author.
E-mail address: L.Susmel@shu.ac.uk (L. Susmel).

https://doi.org/10.1016/j.ijfatigue.2025.109247
Received 6 June 2025; Received in revised form 31 July 2025; Accepted 19 August 2025
Available online 20 August 2025

Nomenclature

Acronyms

EV	Effective Volume
FEA	Finite Element Analysis
GCI	Grey Cast Iron
HCF	High-Cycle Fatigue
HSV	Highly Stressed Volume
SWT	Smith-Watson-Topper
TCD PM	Theory of Critical Distances Point Method
S-N	Stress amplitude vs Number of cycles to failure
a'	Heywood's equation material notch alleviation factor
E	Elastic modulus
F	Bending load
F_{an}	Fatigue average notch effect
K_b	Bending fatigue strength reduction factor, equal to the uniaxial fatigue strength / the bending fatigue strength
K_f	Fatigue strength reduction factor, equal to the un-notched fatigue strength / the notched fatigue strength. May be in terms of net ($K_{f,n}$) or gross ($K_{f,g}$) stress
$K_{f,ES}$	Fatigue strength reduction factor predicted by the Highly Stressed Volume approach, coupled with the Smith-Watson-Topper criterion
$K_{f,He}$	Fatigue strength reduction factor predicted by Heywood's equation
$K_{f,HS}$	Fatigue strength reduction factor predicted by the Highly Stressed Volume approach, coupled with the Smith-Watson-Topper criterion
$K_{f,TS}$	Theory of Critical Distances pseudo fatigue strength reduction factor
K_t	Stress concentration factor, equal to the maximum linear-elastic stress / the net ($K_{t,n}$) or gross stress ($K_{t,g}$)
$K_{t,SWT}$	Stress concentration factor accounting for multiaxial loading using the SWT criterion
ΔK_{th}	Threshold stress intensity factor
k	Negative inverse slope
k_0	Negative inverse slope of the reference SN-curve
L	Critical distance
M_{ES}	Material constant for the Effective Volume approach coupled with the SWT criterion
M_{EV}	Material constant for the Effective Volume approach
M_{HS}	Material constant for the Highly Stressed Volume approach coupled with the SWT criterion
M_{HSV}	Material constant for the Highly Stressed Volume approach
N_A	Number of load cycles to failure at which σ_A is determined
N_f	Number of load cycles to failure
n	Number of non-runout tests
P	Pressure load
P_s	Probability of survival
q	Fatigue notch sensitivity, equal to $(K_f - 1)/(K_t - 1)$
R	Load ratio, equal to minimum applied cyclic stress / maximum applied cyclic stress
r	Notch root radius
T_{RMS}	Mean square error of prediction scatter
t	Time
V	Volume
$V_{95\%}$	Volume of material experiencing a stress $\geq$ 95 % of the maximum stress
V_{eff}	Effective volume
V_i	Volume of element i
$\varepsilon_{n,a}$	Critical plane normal strain amplitude
σ_1	First principal stress
σ_A	High-cycle fatigue refence stress amplitude
σ_a	Stress amplitude
$\sigma_{a,gross}$	Gross stress amplitude
$\sigma_{a,max}$	Maximum stress amplitude
$\sigma_{a(i)}$	Stress amplitude applied during the i-th test
$\sigma_{a,SWT}$	Smith-Watson-Topper equivalent uniaxial fully reversed stress amplitude
$\sigma_{a,SWT,L/2}$	SWT parameter determined at the critical point of the TCD PM
$\sigma_{n,max}$	Critical plane maximum normal stress
σ_{UTS}	Ultimate tensile strength
σ_x, σ_y	Stress acting in the x and y directions, respectively
σ_h	Stress acting in the hoop or circumferential direction
$\Delta\sigma_0$	Stress range at the fatigue limit

factor based on the stress concentration factor, notch root radius, and a material parameter equal to the length of equivalent internal flaws. Heywood's equation has not been validated for notch geometries representative of corroded GCI pipes.

Taylor [19] successfully applied the Theory of Critical Distances (TCD) Point Method (PM) to predict the fatigue response of a notched GCI component to different notch root radii and loadings. The TCD PM shares the theoretical basis of Heywood's [18] approach that the stress some characteristic distance behind the notch root, rather than at the notch root, is the important quantity. Also using the TCD PM, Susmel [20] re-analysed the fatigue data from Taylor et al. [16] with good results, and found that the material characteristic length, L, varied between 3.15 mm and 4.41 mm for load ratios of $R = -1$ to $R = 0.7$.

The notch fatigue behaviour of GCI is thought to be controlled by the distribution of its internal flaws and inclusions [15]. Based on the idea that exposing larger volumes of material to the most damaging stresses increases the likelihood of finding a larger internal flaw, Kuguel [21] proposed the Highly Stressed Volume (HSV) approach to explain the effects of notches, specimen size, and loading types commonly observed in fatigue of engineering metals. Bomas et al. [22] reformulated the empirical HSV approach by combining it with fracture mechanics and a probabilistic model for defect distribution. In this reformulated Effective Volume (EV) approach, the volume parameter is determined using a defined fracture mechanics-derived formula, rather than an arbitrary threshold. The emphasis placed on internal flaws by the HSV and EV approaches mean they have the potential to capture the notch fatigue behaviour of GCI, however neither have been validated for GCI.

The stress histories experienced by in-service GCI water pipes typically feature non-zero mean stresses [10]. Additionally, notches can create localised multiaxial stress fields [15]. Fash and Socie [23] found that the Smith-Watson-Topper (SWT) criterion was also able to account for the mean stress effect for GCI in the High-Cycle Fatigue (HCF) regime. More recently John et al. [24] found that the linear-elastic SWT criterion was also able to predict the un-notched multiaxial fatigue behaviour of GCI due to its extremely low ductility. The linear-elastic SWT criterion is given by [25,26]:

$$\sigma_{a,SWT} = \sqrt{\sigma_{n,max} E \varepsilon_{n,a}} \tag{1}$$

where: $\sigma_{a,SWT}$ is the predicted equivalent uniaxial fully-reversed stress amplitude, $\varepsilon_{n,a}$ is the normal strain amplitude on the critical plane (which in the case of multiaxial stress states can be determined using Hooke's law), and the critical plane is that which experiences the maximum value of $\varepsilon_{n,a}$; $\sigma_{n,max}$ is the maximum value of normal stress on the critical plane; and E is the elastic modulus of the material.

The work detailed in this paper aimed to experimentally investigate the fatigue sensitivity of GCI pipes to localised notches, and bending and biaxal loading, and validate a multiaxial notch fatigue model for GCI. In this study, corrosion pits were assumed to remain constant in size during the accumulation of fatigue damage and to be analogous to geometric notches in a pipe's wall. Therefore, the combination of geometric notches and complex loading make this water industry problem a multiaxial notch fatigue issue. Several potentially suitable notch fatigue models were identified from the literature and calibrated using new data from uniaxial fatigue tests of notched specimens that were manufactured from cast iron pipes. The effectiveness of these calibrated models at predicting the fatigue life of GCI pipes under more realistic conditions was then investigated using new data from novel bending and biaxial fatigue tests of artificially pitted GCI pipe specimens. As well the water pipe application, this work has a strong relevance to other fatigue problems involving thin-walled notched components made of materials that feature inclusions.

2. Notch fatigue modelling approaches for GCI

This section details the four existing notch fatigue models, introduced above, that were tested in this study against experimental fatigue life for notched GCI pipe specimens. These four models are Heywood's equation, the TCD PM, the HSV approach, and the EV approach. The theoretical overview of each model was provided in the introduction, so this section focuses on the mathematical relationships that describe each model. The way in which each model was implemented in the present work is expanded upon further in Section 3.4.

Heywood's equation for GCI is given by [18]:

$$K_{f,He} = \frac{K_t}{1 + 2\left(\frac{K_t - 1}{K_t}\right)\left(\frac{a'}{r}\right)^{1/2}} \tag{2}$$

where: $K_{f,He}$ is Heywood's fatigue strength reduction factor; K_t is the stress concentration factor; r is the notch root radius (mm); and a' is the material notch alleviation factor (mm). Heywood recommended that an a' value of 0.366 mm be used for GCI, based on limited experimental data.

To apply the TCD PM, first the critical distance, L, at the fatigue limit is calculated as [27]:

$$L = \frac{1}{\pi}\left(\frac{\Delta K_{th}}{\Delta \sigma_0}\right)^2 \tag{3}$$

where: ΔK_{th} is the threshold stress intensity factor; and $\Delta\sigma_0$ is the stress range at the fatigue limit. If the linear elastic stress range at the point $L/2$ behind a notch root exceeds $\Delta\sigma_0$, then fatigue failure is predicted. The critical distance varies with cycles to failure, however, Al Zamzami and Susmel [28] successfully analysed fatigue of welded joints, where defects control the fatigue process, using the TCD PM assuming a constant value of L that was independent of fatigue life. To apply the TCD PM to complex three-dimensional notches Louks et al. [29] found it was necessary to test a range of points at a depth of $L/2$ below the stress raiser's surface to identify the critical location.

The HSV approach is typically applied in the following general form [30–32]:

$$\sigma_{A,n} = \sigma_{A,0}\left(\frac{V_{95\%,0}}{V_{95\%}}\right)^{1/M_{HSV}} \tag{4}$$

where: $\sigma_{A,n}$ and $\sigma_{A,0}$ are the high-cycle fatigue refence stress amplitudes of the condition of interest and the reference condition, respectively; $V_{95\%}$ and $V_{95\%,0}$ are the highly-stressed volumes of the condition of interest and reference condition, respectively, that experience a stress $\geq$ 95 % of the maximum stress; and M_{HSV} is a material constant. The 95 % threshold is arbitrary, and some authors have used other thresholds such as 80 % [31].

Using the EV approach of Bomas et al. [22] the high-cycle fatigue refence stress amplitude of a given geometry and load type, $\sigma_{A,n}$, in terms of maximum linear elastic stress is calculated as follows:

$$\sigma_{A,n} = \sigma_{A,0}\left(\frac{V_{eff,0}}{V_{eff}}\right)^{1/M_{EV}} \tag{5}$$

where: $\sigma_{A,0}$ is the fatigue limit of the reference condition in terms of maximum linear-elastic stress; $V_{eff,0}$ is the effective volume of the reference condition; V_{eff} is the effective volume of the condition of interest; and M_{EV} is a material parameter which is related to the defect size distribution and fracture mechanics properties of the material. For a given geometry and load condition, the effective volume is calculated as follows [22]:

$$V_{eff} = \int_V \left(\frac{\sigma_a(x,y,z)}{\sigma_{a,max}}\right)^{M_{EV}} dV \tag{6}$$

where: $\sigma_a(x,y,z)$ is the stress amplitude at any coordinate point x, y, z within the material; and $\sigma_{a,max}$ is the maximum stress amplitude occurring at any point within the material. The stress amplitude used in Eqs. (4) and (5) may be a principal stress amplitude, or the amplitude of some equivalent stress.

3. Methods

To calibrate and test the ability of the notch fatigue models introduced in the previous section to estimate the fatigue lives of GCI water pipes new experimental fatigue data were obtained. Specifically, high-cycle fatigue data was needed for GCI water pipes featuring localised corrosion pitting and exposed to multiaxial loading. Following the fatigue tests, Finite Element Analysis (FEA) was used to estimate the stress parameters required as inputs for the notch fatigue models (e.g. K_t). This section details the fatigue tests performed and the analysis techniques used to implement and test each notch fatigue model.

To calibrate each of the notch fatigue models the S-N curves of a notched and an un-notched specimen under the same loading type are needed. Therefore, uniaxial $R = -1$ fatigue tests of specimens featuring a sharp circumferential notch were conducted which could be used with the un-notched $R = -1$ fatigue data reported in ref [24] to calibrate the models.

To test the validity of the notch fatigue models a series of further tests were conducted that investigated the effects of notch root radius, bending loading, localised pitting, and biaxial loading. Note that biaxial stress states feature two non-zero principal stresses, while the third principal stress is zero. These variables were highly relevant to the water pipe application, so it was important that the notch fatigue models were able to account for these effects. Given the number of variables, several sets of fatigue tests were performed using different combinations of specimen geometry and loading.

3.1. Materials

Approximately 40 fatigue specimens were required to conduct the fatigue test programme set out in this paper. To allow this number of tests using full sections of pipe barrel, and to reduce specimen-to-specimen mechanical property variation relative to testing exhumed pipes, specimens were manufactured from new DN50 BS416-2 [33] GCI pipes. The graphite microstructure, tensile strength, and uniaxial fatigue behaviour of these BS416-2 pipes are within the range expected for GCI water pipes, enabling them to represent GCI water pipes in small-scale destructive tests [24,34]. These pipes have an average tensile strength of 229 MPa and average elastic modulus of 82 GPa [34]. Similarly to real GCI water pipes, the manufacturing process used to produce BS416-2 pipes is not tightly controlled, resulting in a substantial variation in fatigue strength between nominally identical specimens [34].

To calibrate the notch fatigue models and investigate the effect of notch root radius, two designs of circumferentially notched uniaxial specimens were tested: one with a nominal 0.4 mm root radius and 35° flank angle (Fig. 1a) and one with a nominal 5.0 mm root radius (Fig. 1b). The remaining wall thickness behind the notch root was approximately 1.8 mm for all specimens, which is relatively thin but representative of the water pipe application.

To investigate the interacting effects of bending loading, localised pitting, and biaxial loading, un-notched specimens and specimens featuring localised notches were tested. The un-notched specimens (Fig. 2a) featured a gauge section with a large transition radius to ensure failure occurred in the centre of the specimen. The notched bending specimens had local notches with a round plan cut into them, as shown by Fig. 2b and 2c. Two designs of notched bending specimens were tested: one with a nominal 0.1 mm root radius, 90° flank angle notch, and one with a nominal 4 mm root radius notch. The remaining wall thickness at the gauge section for these specimens was also approximately 1.8 mm.

3.2. Fatigue tests

A list of specimen and load combinations used to obtain the fatigue data for this work is provided in Table 1 as a reference for readers. To characterise the fatigue curves of the circumferentially notched specimens, 10 specimens were tested across 5 stress levels, giving 50 % replication. These uniaxial tests were run under load control at 8 Hz using a Schenke servo-hydraulic rig fitted with shaft clamps that were able to firmly hold the fatigue specimens during tests (see Fig. 3a and 3b). 2×10^6 cycles was the runout definition. Due to the rapid crack propagation observed, failure was defined as specimen separation shown by Fig. 3a and 3b.

The bending and biaxial fatigue tests were used to explore the effects of different fatigue loads on the fatigue life of notched GCI pipes. To reflect realistic loading of GCI water pipes, bending and internal water pressure loading were used to apply biaxial stress states. Fig. 4a, 4b, and 4c illustrate how combined bending and internal water pressure loading can be used to create a biaxial stress state at the invert (bottom) midpoint of a pipe specimen. This was possible because the axial stress is primarily a function of the bending load whereas the circumferential stress is primarily a function of the internal pressure load. For the multiaxial fatigue loading tests, 180° out-of-phase biaxial loading was selected to represent a worst-case loading because previous fatigue tests of un-notched GCI specimens have shown that torsional loading is more damaging than uniaxial loading, from a normal stress amplitude perspective [24].

(a) Sharp notch uniaxial specimen

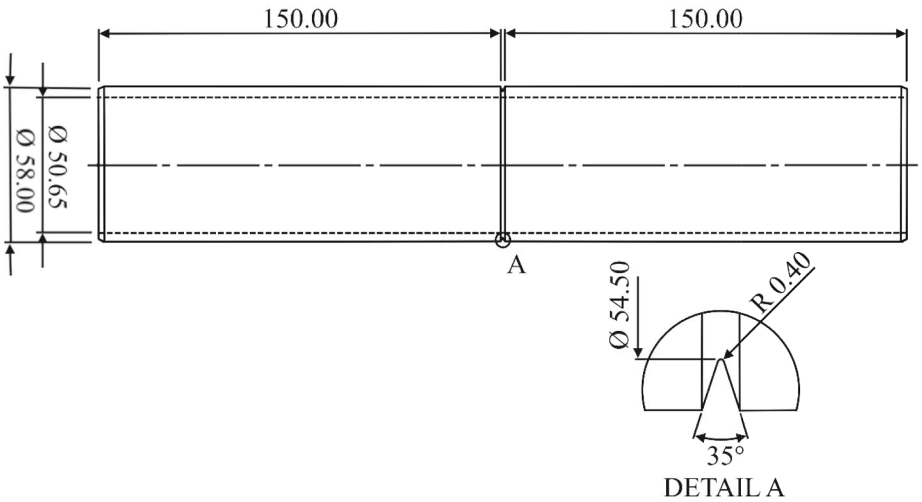

(b) Blunt notch uniaxial specimen

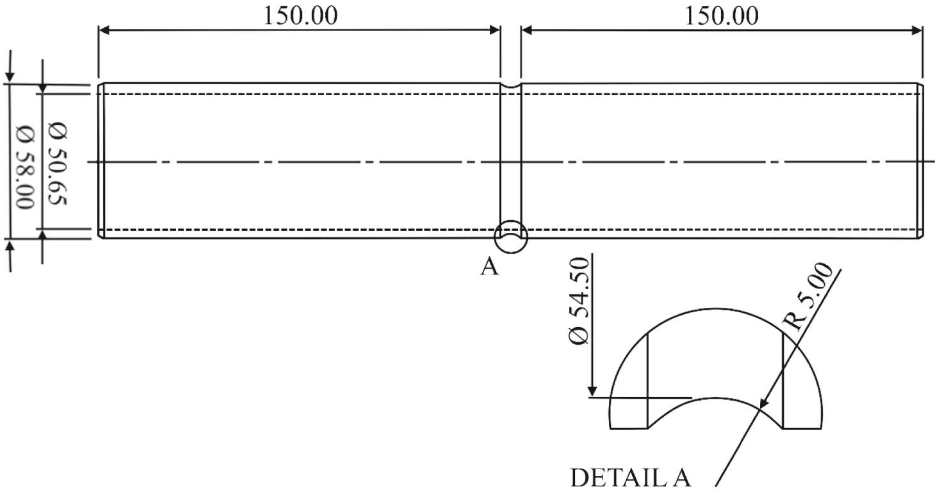

Fig. 1. Uniaxial fatigue specimen dimensions, highlighting the two different circumferential notches tested.

(a) Un-notched specimen

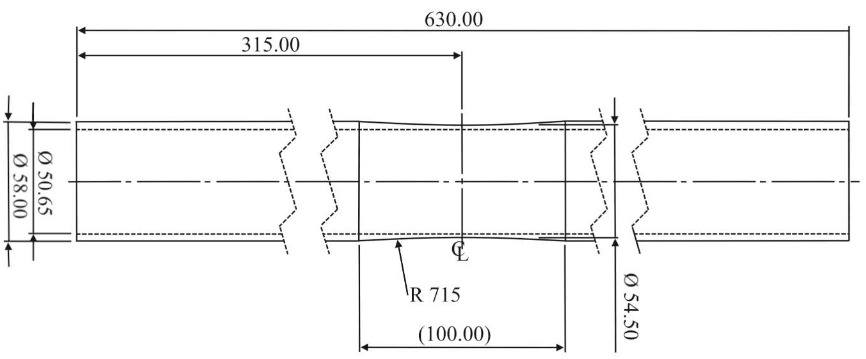

(b) Sharp circular notch specimen

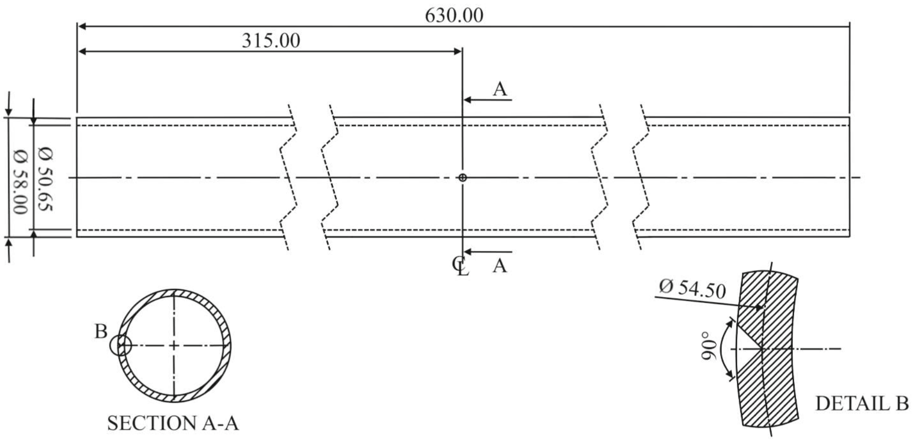

(c) Blunt circular notch specimen

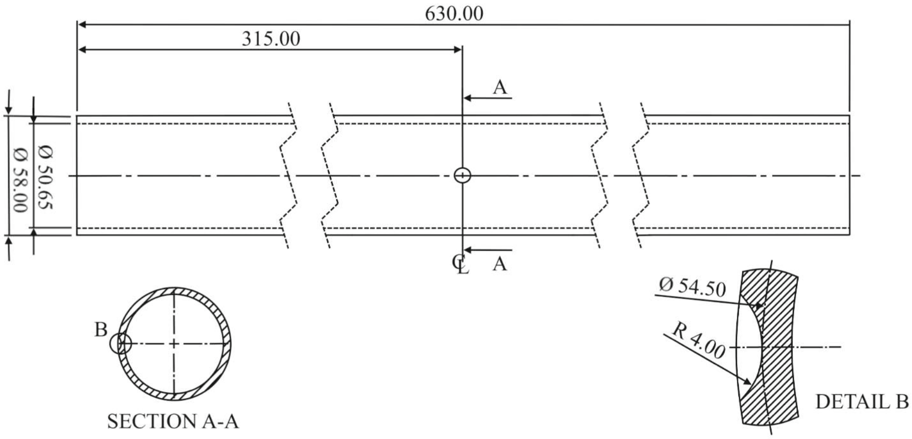

Fig. 2. Dimensions of the fatigue specimens used in the bending and biaxial fatigue tests.

For the bending and biaxial fatigue tests, the specimens were tested under four-point bending so that failures would occur in the region of uniform bending stress away from the influence of the load points. The bending and biaxial fatigue tests were conducted using new test equipment illustrated by Fig. 4d. To provide the bending load application force, this test equipment was positioned within a servo-hydraulic uniaxial fatigue test machine. For the biaxial tests, the internal water pressure load was applied by a bespoke hydraulic system that was connected to specimens via the hose visible on the right of Fig. 4d. This new experiment was robustly tested to verify its ability to apply the intended cyclic stresses to specimens [35]. The greatest total bending load amplitude applied during a test was 8.7 kN, whereas the greatest internal pressure load amplitude used was 6.3 MPa. Real-world bending fatigue loading of small diameter pipes is likely to feature a mean stress, so a load ratio of 0.1 was used for all bending fatigue tests.

The bending fatigue tests aimed to provide data against which the models could be tested, and to characterise the approximate slope and position of the SN curves. Therefore, four specimens were tested across two stress levels. Tests were run under load control at 4 Hz and 6×10^5 cycles was the runout definition as very few uniaxial failures occurred after this number of cycles. Failure was defined as the formation of a leaking through-wall crack, which was detected by measuring the

Table 1
List of fatigue test sets, detailing the combination of specimen design and applied loading. Reference codes used to abbreviate these test sets for tables and figure legends are also provided.

Specimen type	Loading	Reference
Un-notched	Uniaxial, R = -1	UN-UR-1*
Un-notched	Uniaxial, R = 0.1	UN-UR-0.1*
Sharp notch, Fig. 1a	Uniaxial, R = -1	SN-UR-1
Blunt notch, Fig. 1b	Uniaxial, R = -1	BN-UR-1
Un-notched, Fig. 2a	Four-point bending, R = 0.1	UN-4B
Sharp circular notch, Fig. 2b	Four-point bending, R = 0.1	SCN-4B
Blunt circular notch, Fig. 2c	Four-point bending, R = 0.1	BCN-4B
Un-notched, Fig. 2a	Bending and internal pressure, 180° out-of-phase (BP), R≈0.1	UN-BP
Sharp circular notch, Fig. 2b	Bending and internal pressure, 180° out-of-phase (BP), R≈0.1	SCN-BP

*Reported in [24] and used as reference curves in the present work.

pressure drop of pressurised water sealed within the specimens.

The consistent negative inverse slope obtained for the uniaxial and bending loading data sets meant it was possible to characterise the behaviour of the multiaxial loading sets by testing specimens at a single stress level. For each biaxial test set three specimens were tested at a single stress level with a target of 5 × 10^3 cycles to failure and a run-out limit of 1 × 10^5 load cycles. This run-out limit was based on the 10 % probability of survival interval determined for un-notched specimens under uniaxial loading. The combined bending and internal water pressure loading was applied at 1.7 Hz, limited by the controller speed. To cause true biaxial failures the bending and internal pressure stress amplitudes applied were set to be approximately equally damaging, although equipment constraints meant the load ratio of the axial stress component was around 0.4 instead of 0.1. Failure for these tests was also defined as the formation of a leaking through-wall crack and a high-speed camera was used to detect this.

3.3. Fatigue data analysis

Before the notch fatigue models could be applied to the experimental fatigue data, several parameters were calculated to characterise each data set. The net stresses applied to the uniaxial specimens were calculated as the applied force divided by the net area. The areas were determined from post-test measurements to account for small geometry variations between specimens. The net and gross stresses applied to the bending and biaxial loading specimens were determined using the FEA procedure described below.

The least squares method was used to estimate the relationship between stress amplitude and cycles to failure according to ASTM E739-10 [36] for each un-notched and sharp notch uniaxial and bending data set as these each contained a sufficient range of stress levels. The least squares estimate corresponds to the 50 % probability of survival estimate ($P_S = 50\%$). To indicate the range of expected fatigue strengths, the 10 % and 90 % probability of survival scatter bands were calculated at a 95 % confidence level for the un-notched uniaxial data according to ASTM STP91 [37]. Scatter bands were not calculated for the other data sets because they contained insufficient data points.

To estimate the fatigue strength reduction factor associated with each data set, regardless of whether the $P_S = 50$ % fatigue curve was available, a new parameter was defined that exploits the very similar negative inverse slopes of the notched and un-notched data sets obtained for this study. This new parameter, the fatigue average notch effect, F_{an}, is effectively the average fatigue strength reduction factor obtained by estimating σ_A associated with each experimental data point using the negative inverse slope of the un-notched uniaxial case:

$$F_{an} = \frac{1}{n}\sum_{i=1}^{n}\left\{\frac{\sigma_{A,o}}{\sigma_{a(i)}\left[\frac{N_{f(i)}}{N_A}\right]^{1/k_0}}\right\} \tag{7}$$

(a) Sharp notch uniaxial specimen (b) Blunt notch uniaxial specimen

(c) Un-notched bending specimen (d) Sharp notch bending specimen

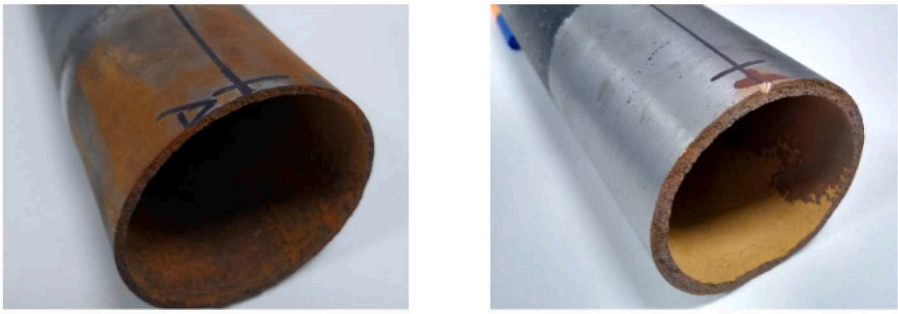

Fig. 3. Examples of fractured specimens post-test including (a-b) uniaxial specimens still secured in the fatigue test machine, and (c-d) the circumferential fractures observed at the midpoint of specimens subjected to bending fatigue loads.

(a) Internal pressure load schematic (b) Four-point bending load schematic

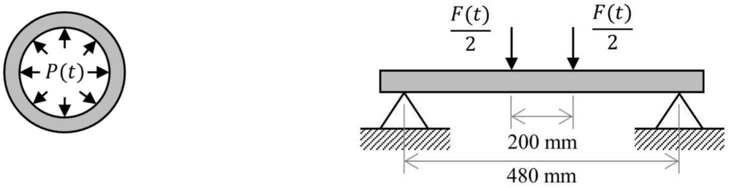

(c) Pipe invert principal stresses (d) Combined four-point bending and internal pressure loading equipment with pipe specimen

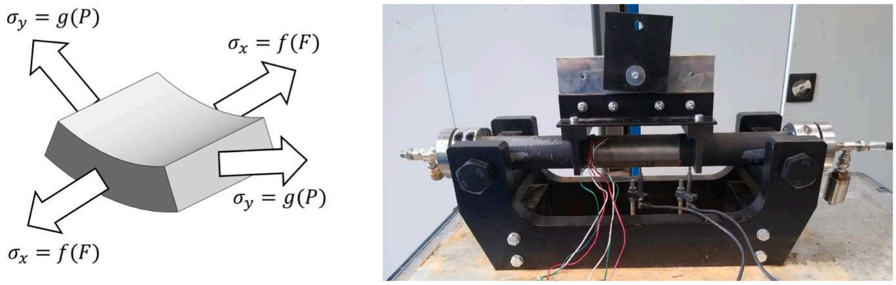

Fig. 4. Diagrams (a-c) showing how combined bending and internal pressure loading can be used to create a biaxial stress state at the invert (bottom) midpoint of a pipe specimen, and a photograph (d) of the equipment used to apply these loads (note that the photograph was staged outside the fatigue machine to give an unobstructed view).

where: n is the number of non-runout tests in the data set; $\sigma_{a(i)}$ is the stress amplitude applied during the i-th test; $N_{f(i)}$ is the observed cycles to failure of the i-th test; and k_0 is the negative inverse slope of the un-notched uniaxial case. F_{an} was always calculated in terms of net stresses. To enable the significance of any differences in F_{an} to be determined, the 90 % confidence interval associated with each fatigue average notch effect value was calculated as detailed in [38].

3.4. Fatigue life estimates

While Section 2 outlined the mathematical relationships behind each notch fatigue approach, applying these models in practice required some additional considerations which are detailed here. Additionally, to test the idea that the material was insensitive to the presence of notches, or to notch geometry, fatigue life predictions were made using the SWT criterion (Eq. (1) applied to the gross and net stress amplitudes and referenced to un-notched $P_S = 50\%$ curves for the relevant loading type.

To make predictions using Heywood's equation (Eq. (2) K_t values were calculated for each specimen and load combination using FEA. The uniaxial sharp notch data was used to calibrate Heywood's equation, giving $a' = 1.35$ mm. Estimated fatigue strength reduction values calculated for each notched data set are given in Table 2. To enable Heywood's equation to be applied to data sets featuring mean and multiaxial stresses the SWT criterion was used to determine the effective gross stress.

To apply the TCD PM, the stress state at a depth of $L/2$ behind the notch was estimated for each specimen geometry and load combination using FEA. The slopes of the uniaxial un-notched and sharp notch fatigue curves used for calibration were very similar, so L was assumed to be independent of fatigue life. L was calculated by comparing the notched and un-notched fatigue strengths at 10^6 cycles to failure, resulting in $L = 0.87mm$. For the localised pit specimens, the stress state was determined at a range of points at a depth of L and the most damaging stress state amongst these points taken as the critical location, as recommended by Louks et al. [29]. The assumption of constant L meant a pseudo fatigue strength reduction factor for the combined TCD PM and SWT criterion could be calculated:

$$K_{f,TS} = \frac{\sigma_{a,SWT,L/2}}{\sigma_{a,gross}}$$

where: $\sigma_{a,gross}$ is the applied gross stress amplitude; and $\sigma_{a,SWT,L/2}$ is the SWT parameter determined at the critical point of the TCD PM when the specimen is subject to the same gross stresses.

To apply the HSV and EV methods in conjunction with the SWT criterion as a fatigue strength reduction factor, Eqs. (4) and (5) were modified as follows:

Table 2

Notch fatigue analysis parameters determined for each test set as described in Sections 3.4 and 3.5. The values reported here correspond to the median specimen geometry of each test set and are given in terms of gross stress, except for the uniaxial sets where the net stress values are more representative. $V_{95\%}$ and V_{eff} are both in terms of $\sigma_{a,SWT}$ for all test sets.

Test set	r (mm)	$K_{t,g}$	$K_{t,n}$	$K_{f,He}$	$K_{f,TS}$	$K_{t,SWT}$	$V_{95\%}$(mm^3)	$K_{f,HS}$	V_{eff}(mm^3)	$K_{f,ES}$
UN-UR-1	–	1	1	–	1	1	$1.09\bullet10^4$	1.00	$1.30\bullet10^4$	1.00
UN-UR-0.1	–	1	1	–	1.49	1.49	$1.09\bullet10^4$	1.49	$1.30\bullet10^4$	1.49
SN-UR-1$^+$	0.40	9.09	4.5	1.17	1.17	4.32	$2.09\bullet10^{-1}$	1.17	$1.57\bullet10^0$	1.17
BN-UR-1$^+$	5.12	4.33	2.03	1.33	1.3	1.94	$6.96\bullet10^0$	0.80	$4.75\bullet10^1$	0.86
UN-4B	–	1	1	–	1.49	1.5	$3.16\bullet10^2$	0.98	$1.38\bullet10^3$	1.09
SCN-4B	0.27	3.15	1.77	0.77	2.01	4.59	$1.93\bullet10^{-4}$	0.53	$2.79\bullet10^0$	1.35
BCN-4B	3.47	2.06	1.16	1.25	2.21	3.03	$1.03\bullet10^{-1}$	0.75	$5.09\bullet10^1$	1.36
UN-BP	–	1.00	1.00	–	2.22	2.22	$2.12\bullet10^2$	1.38	$1.16\bullet10^3$	1.56
SCN-BP*	0.27	3.20/ 3.48	1.79/ 1.85	0.78/ 0.83	1.90	4.50	$1.17\bullet10^{-4}$	0.49	$2.89\bullet10^0$	1.33

*$K_{t,g}$, $K_{t,n}$ and $K_{f,He}$ values for: axial stress / hoop stress.

$^+$ Parameters in terms of net stress rather than gross stress.

$$K_{f,HS} = K_{t,SWT}\left(\frac{V_{95\%,SWT,0}}{V_{95\%},SWT}\right)^{-1/M_{HS}} \tag{8}$$

$$K_{f,ES} = K_{t,SWT}\left(\frac{V_{eff,SWT,0}}{V_{eff},SWT}\right)^{-1/M_{ES}} \tag{9}$$

Where $K_{t,SWT} = \sigma_{a,SWT,max}/\sigma_{a,gross}$, which is the gross stress concentration factor accounting for multiaxial loading using the SWT criterion determined using the maximum value of the SWT criterion at the notch and the gross stress amplitude. $V_{95\%,SWT}$ and $V_{eff,SWT}$, the highly stressed and effective volumes in terms the SWT criterion, were calculated using FEA. $V_{95\%,SWT}$ was calculated by summing the volume of the elements experiencing $\geq$ 95 % of the maximum value of the SWT criterion, whereas the integral used to calculate $V_{eff,SWT}$ was approximated as:

$$V_{eff,SWT} = \sum_{i=1}^{n}\left[\left(\frac{\sigma_{a,SWT,i}}{\sigma_{a,SWT,max}}\right)^{M_{ES}} V_i\right] \tag{10}$$

where: n is the number of elements in the FEA model; $\sigma_{a,SWT,i}$ is the SWT equivalent stress amplitude experienced by element i, calculated using Eq. (1); $\sigma_{a,SWT,max}$ is the greatest SWT equivalent stress amplitude experienced by any element in the FEA model; and V_i is the volume of element i. Through comparing the uniaxial fully reversed un-notched fatigue curve and sharp circumferential notch fatigue curve, M_{HS} and $V_{95\%,SWT,0}$ were calculated to be 8.31 and 10,930 mm^3, respectively. Given the dependency of $V_{eff,SWT}$ on the material constant M_{ES} (see Eq. (6)), M_{ES} was determined through a trial and improvement process, using the same data sets as for the HSV material constant M_{HS}. M_{ES} and $V_{eff,SWT,0}$ were calculated to be 6.90 and 13,020 mm^3, respectively. The prediction accuracy of each approach detailed in this section was quantified using the mean square error quantity, T_{RMS}, as explained by Walat and Lagoda [39].

3.5. Finite element analysis

Linear-elastic FEA was used to calculate the local stress quantities required by the fatigue life estimation methods described in the previous section. To do this, finite element models were created and solved for each of the specimen-load combinations detailed in Table 1. For example, to calculate the effective volume, $V_{eff,SWT}$, for a test set the stress estimates for each element in the corresponding finite element model were inputted to Eq. (10). A benefit of using linear-elastic models was that only one static load condition needed to be modelled for each specimen-load combination, and the resultant stress could be scaled linearly with load to determine cyclic parameters such as stress amplitude.

The uniaxial specimens were modelled as two-dimensional axisymmetric problems for computational efficiency (Fig. 5a) using first-order quadrilateral elements. To model the notched uniaxial specimens (Fig. 1), the uniformly reduced gauge section shown in Fig. 5a was replaced with the notch geometry. A sub-model region at the notch root was used to capture the local stress distribution in detail (Fig. 5b).

The bending and multiaxial specimens (Fig. 2) required three-dimensional models due to the complexity of the boundary conditions and specimen geometry. However, these models' sizes were reduced by taking advantage of two planes of symmetry to create a quarter-pipe model, shown by Fig. 6a. The quarter-pipe model boundary conditions, shown by Fig. 6b, were selected to closely replicate the experimental arrangement shown by Fig. 4d. These boundary conditions were validated against strain and displacement measurements taken from the experiment for the full range of loading conditions used in tests; the FEA predictions matched the experimental values within ± 10 % showing the validity of these boundary conditions [35]. Hexahedral elements were used for the main body of these models and for the gauge section of the un-notched models, as shown by Fig. 6c. However, it was necessary to use tetrahedral elements in the vicinity of notches to capture the more

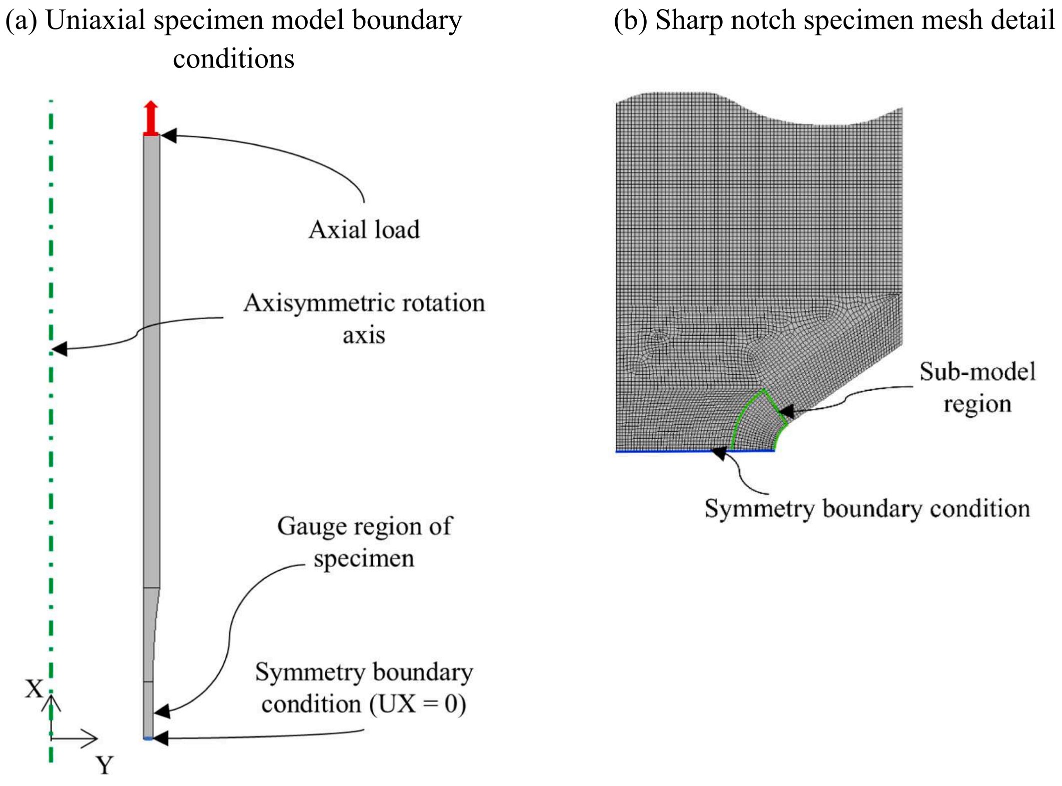

Fig. 5. Illustration of the FEA modelling approach adopted for the uniaxial fatigue tests, showing: (a) the boundary conditions applied to the 2D axisymmetric model (un-notched specimen model shown), and (b) detail of the mesh for the sharp notch specimen gauge section.

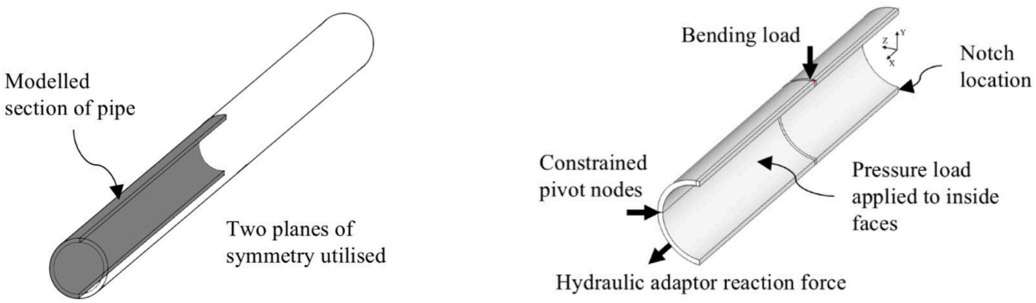
(a) Pipe modelling approach

(b) Quarter-pipe model boundary conditions

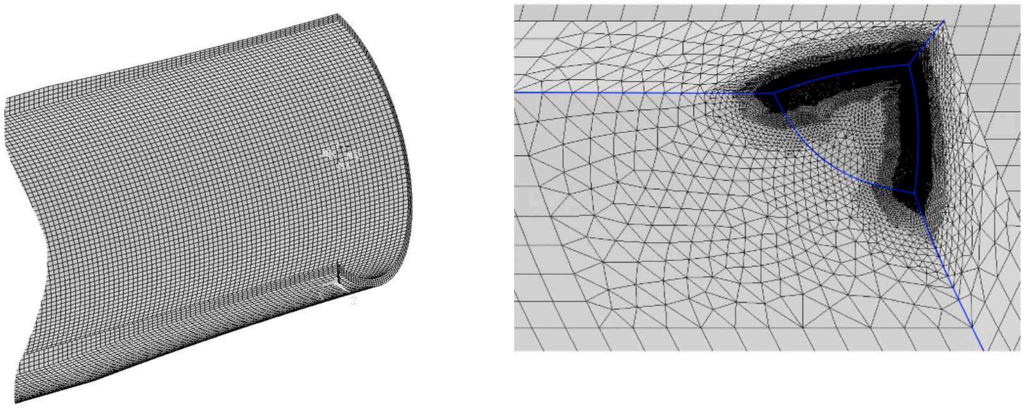
(c) Un-notched gauge section mesh

(d) Blunt circular notch mesh detail

Fig. 6. Illustration of the FEA modelling approach adopted for the bending and internal pressure fatigue tests, showing: (a) the modelled region of the pipe, (b) the boundary conditions applied to the quarter pipe model (note that appropriate symmetry boundary conditions were also applied), and (c-d) details of the gauge section mesh for the un-notched and blunt circular notch specimen types. The blue lines on sub-figure (d) indicate the location of geometry edges obscured by the refined mesh.

complex geometry, as illustrated by Fig. 6d for the blunt circular notch.

For both model types, the mesh was refined in the critical region of each model until the K_f values calculated using the methods detailed in Section 3.4 converged to within ± 1 % over two subsequent iterations. The layered mesh refinement approach can be seen in Fig. 6d. Convergence was not possible for the HSV method for the sharp circular notch specimens under biaxial loading. Examples of element sizes that achieved convergence are 0.5 mm for the un-notched specimens, 0.02 mm for the sharp circular notch specimens, and 0.001 mm for the sharp circumferential notch specimens.

4. Results

This section details the outcomes of the uniaxial, bending, and biaxial fatigue tests and presents analysis used to assess the significance of the load and notch effects observed in this data. Additionally, the fatigue life estimation performance of the notch fatigue models is compared with the experimental data.

4.1. Uniaxial fatigue tests

The notched uniaxial fatigue specimens failed suddenly with separation occurring over a single load cycle, indicating rapid crack propagation. Failures initiated at the notch root stress concentration and the fracture surfaces of both the sharp and blunt notch specimens lay on the plane of maximum normal stress amplitude, as shown by Fig. 3a and 3b, implying a tensile cracking mechanism.

The notched uniaxial fatigue results are plotted in Fig. 7. The data display significant scattering, however, this was expected given inclusions found in the specimen material. Three blunt notch specimens survived 2×10^6 load cycles and were classed as runouts. These blunt notch runouts were all tested at stress levels that caused failure before 2×10^6 load cycles for the un-notched and sharp notch specimens. This indicates that for the blunt notch specimens the location of the S-N curve "knee point" marking the transition from high-cycle to very high-cycle fatigue occurred at a much lower number of cycles to failure than the un-notched or sharp notch specimens, although further tests are required to confirm this.

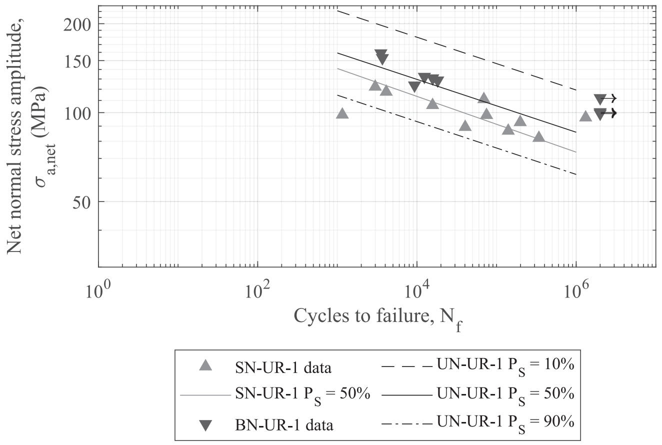

Fig. 7. Uniaxial R = -1 loading fatigue data and fitted curves illustrating the effect of sharp and blunt notches relative to the un-notched case. The data sets shown are sharp notch specimens (SN-UR-1), blunt notch specimens (BN-UR-1), and un-notched uniaxial (UN-UR-1) from [24] are included for reference. To show the notched data more clearly, only the 10 %, 50 %, and 90 % probability of survival curves for the un-notched data are plotted.

The blunt notch specimens had fatigue strengths very close to the un-notched 50 % probability of survival curve, but the sharp notch specimens generally had lower fatigue strengths which fell between the un-notched 50 % and 90 % probability of survival curves. This indicates some sensitivity to notch root radius, although all the notched uniaxial data, except one, fell within the un-notched uniaxial scatter bands.

Failure data for a wide range of stress levels were available for the sharp notch fatigue tests enabling the 50 % probability of survival curve parameters to be calculated, as shown in Fig. 7 and Table 3. The 50 % probability of survival curve was not calculated for the blunt notch data set because the stress amplitude range over which valid results were available was too small to give a representative curve. The average $K_{f,n}$ and $K_{f,g}$ values for both data sets are also included in Table 3, which again show a small difference between the two notch types. Note the similarity between the $K_{f,n}$ and F_{an} values shown in Table 3, indicating that F_{an} provided a good approximation of $K_{f,n}$.

4.2. *Bending and biaxial fatigue tests*

The bending and biaxial (180° out-of-phase bending and internal pressure loading) fatigue results are plotted in Figs. 8 and 9, respectively. Note that the cycles to failure of the un-notched biaxial fatigue tests were previously reported in [35] as part of the experimental method verification, however, the stress-levels tested have not previously been reported. All specimens failed by developing a circumferential crack, as shown by Fig. 3c and 3d, which suggests the final tensile crack growth stage was driven by the axial bending stress. The S-N curve parameters, where available, and the calculated F_{an} values are provided in Table 3.

The un-notched bending tests demonstrated higher fatigue strengths than the un-notched uniaxial case for the same stress ratio (R = 0.1) and all un-notched bending fatigue data fell outside the uniaxial scatter bands, highlighting the significance of this effect. Both sharp ($r = 0.27mm$) and blunt ($r = 3.5mm$) circular notches reduced the bending fatigue strength relative to the un-notched case. The sharp and blunt circular notch specimens had similar fatigue strengths, indicating that the notch root radius had a low impact. However, like the uniaxial blunt notch tests, two blunt notch bending tests survived 6×10^5 cycles at stress amplitudes that caused sharp notch specimens to fail suggesting some difference in fatigue behaviour.

For the un-notched biaxial fatigue tests, three specimens were tested with gross stress amplitudes of about 70 MPa in both the hoop and axial directions, and stress ratios of 0.12 and 0.41, respectively. This loading was selected with the aim of each stress direction being equally damaging. Two specimens failed before the un-notched uniaxial $P_S = 90\%$ curve was reached, whereas one specimen survived 10^5 load cycles and was classed as a runout, resulting in a very scattered data set.

Tests of the sharp, circular notch specimens under 180° out-of-phase biaxial loading were run with the maximum possible bending and internal water pressure load amplitudes. One specimen survived 10^6 cycles before failing at a pipe support, and the remaining two specimens tested both failed at a hydraulic adapter after about 6×10^4 load cycles. Due to the high likelihood of unintended failure types caused by the high loading amplitudes, further tests of this type were not run. These effective runouts were used to determine a lower-bound fatigue average notch effect. From a gross axial stress amplitude perspective, the sharp circular notch was less damaging under 180° out-of-phase biaxial loading than no notch.

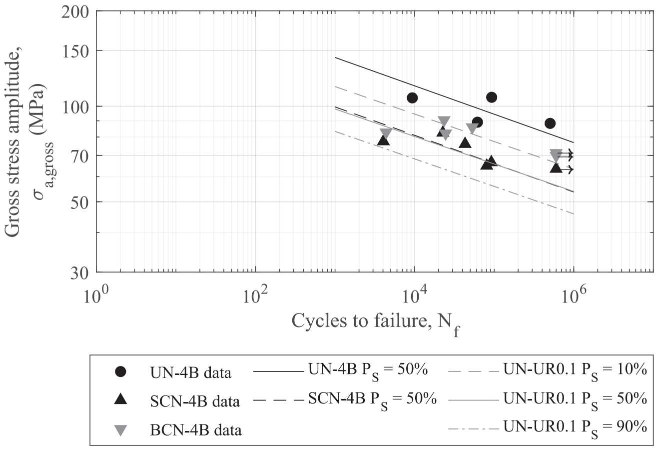

Fig. 8. Bending R = 0.1 and uniaxial R = 0.1 loading fatigue data and fitted curves illustrating the effect of bending loading with and without notches relative to un-notched specimens subject to uniaxial loading. The bending loading data sets shown are un-notched specimens (UN-4B), sharp circular notch specimens (SCN-4B), and blunt circular notch specimens (SCN-4B). The un-notched uniaxial R = 0.1 (UN-UR0.1) S-N curves from [24] are provided for reference.

4.3. *Effect of loading and notches on fatigue strength*

To identify which of the investigated fatigue load and notch types had a significant effect on the fatigue strength of the GCI pipe specimens, the high-cycle reference stress amplitude confidence intervals of the data sets were compared using t-tests. Fig. 10 shows the average reference stress amplitudes, calculated at 10^6 cycles, and 90 % confidence intervals for a selection of un-notched fatigue data sets. Table 4 shows the results of the t-tests in terms of the p-values calculated and whether the null hypothesis was rejected at a 90 % confidence level; in all four un-notched cases the null hypothesis was rejected indicating different average reference stress amplitudes. Therefore the 43 % average increase in fatigue strength caused by bending loading, and the 28 % average reduction in fatigue strength caused by out-of-phase bending and internal pressure loading, relative to uniaxial $R = 0.1$ loading, were statistically significant.

To determine the significance of the notch effect in each data set, the net stress concentration factor for each notched specimen type, calculated using FEA, is plotted against the fatigue average notch effect in Fig. 11 and the *t*-test results are provided in Table 4. These F_{an} values account for the effect of bending fatigue loading so allow direct

Table 3
Parameters describing the linear S-N curve and fatigue notch effect for each fatigue data set. The average measured notch root radius values are provided. Some data sets did not contain a sufficient range of stress levels to allow calculation of the S-N curve parameters, but the notch effect was characterised for all data sets using F_{an}.

Test set	r (mm)	n	Runouts	R	k	σ_A(MPa)	$\frac{\sigma_A}{\sigma_{UTS}}$	$K_{f,g}$	$K_{f,n}$	F_{an}
SN-UR-1	0.40	11	0	−1.00	10.6	73.5	0.32	2.61	1.17	1.16
BN-UR-1	5.12	6	3	−1.00	–	–	–	–	–	0.96
UN-4B	–	4	0	0.10	11.2	76.8	0.34	0.70	0.70	0.70
SCN-4B	0.27	5	1	0.10	11.2	53.7	0.23	1.43	0.89	0.77
BCN-4B	3.47	4	2	0.10	–	–	–	–	–	0.74
UN-BP*	–	2	1	0.41 / 0.12	–	–	–	–	–	1.88 / 1.38
SCN-BP*	0.27	0	3	0.36 / 0.10	–	–	–	–	–	<1.10 / <0.83

*R and F_{an} values for: axial stress / hoop stress.

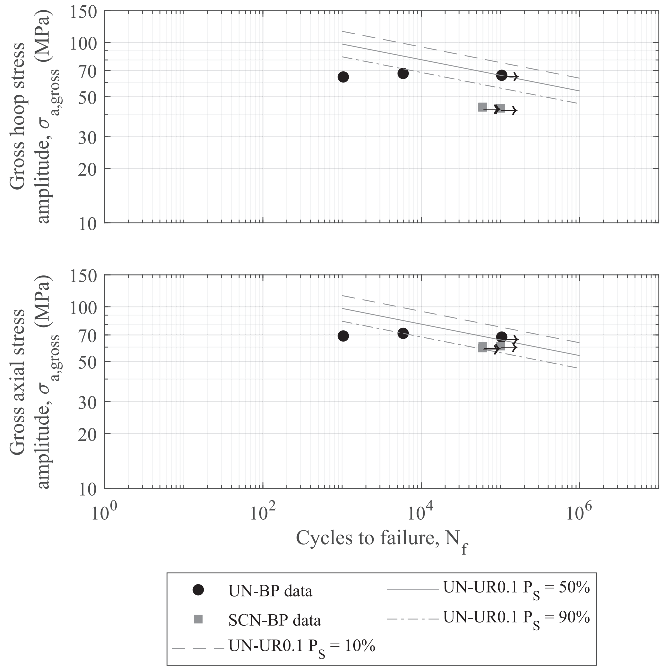

Fig. 9. 180° out-of-phase biaxial loading fatigue data illustrating the effect of biaxial loading on notched and un-notched specimens relative to uniaxial loading with a similar load ratio. The biaxial data sets shown are un-notched specimens (UN-BP) and sharp circular notch specimens (SCN-BP). The un-notched uniaxial R = 0.1 (UN-UR0.1) curves from [24] are provided for reference.

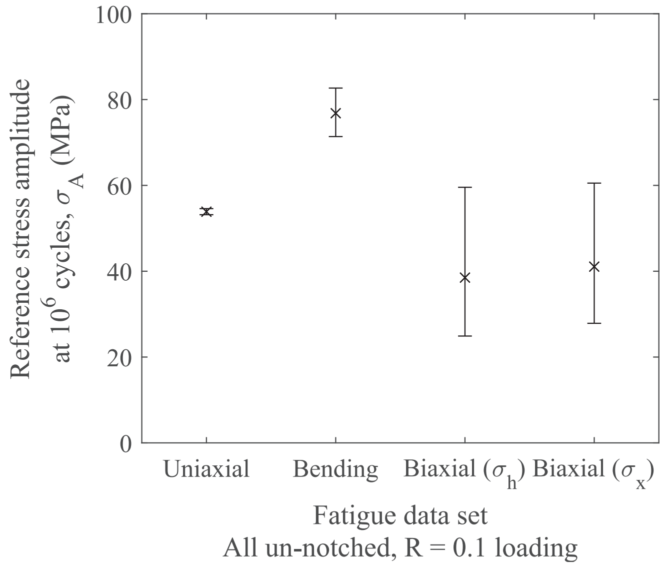

Fig. 10. Plot of mean reference stress amplitude (at 10^6 cycles) and 90 % confidence intervals for un-notched fatigue data sets under R = 0.1 loading, illustrating the effects of bending and 180° out-of-phase biaxial loading relative to uniaxial loading. The test sets shown are un-notched uniaxial R = 0.1 (UN-UR0.1) from [24], un-notched bending (UN-4B), and un-notched biaxial (UN-BP).

Table 4
Results of the t-tests used to compare the fatigue data sets, where 'Reject' indicates there is a statistically significant difference between the compared sets. For the un-notched data, the null hypothesis was that the two data sets compared had the same reference stress amplitudes. For the notched data, the null hypothesis was that the two data sets compared had the same F_{an} values.

Fatigue data sets compared	p-value	Accept or reject null hypothesis at 90 % confidence level
UN-UR0.1 & UN-4B	0.000	Reject
UN-UR0.1 & UN-BP (σ_h)	0.000	Reject
UN-UR0.1 & UN-BP (σ_x)	0.001	Reject
UN-UR-1 & SN-UR-1	0.037	Reject
UN-UR-1 & BN-UR-1	0.410	Accept
UN-UR-1 & SCN-4B	0.003	Reject
UN-UR-1 & BCN-4B	0.003	Reject
SCN-4B & BCN-4B	0.502	Accept

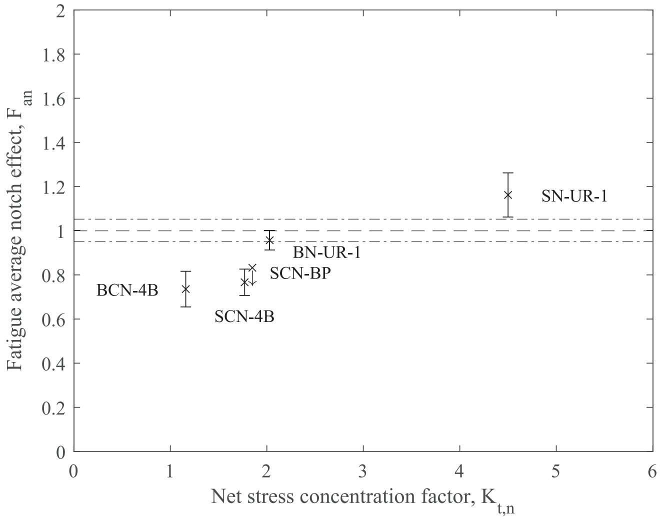

Fig. 11. Plot of F_{an} vs. mean $K_{t,n}$ for all notched data sets, including the 90 % confidence intervals, illustrating the relationship between the notches' stress concentration and effect on fatigue strength. The equivalent position of the unnotched uniaxial R = −1 90 % confidence interval from [24] is marked with chain lines. Downward arrows indicate data sets containing a substantial proportion of runout tests.

comparison of the effect of notch shape. Comparing K_t and F_{an} in terms of the net stresses rather than the gross stresses allowed the effect of specimen-to-specimen variations in wall thickness to be excluded. The biaxial data set included in Fig. 11 is plotted in terms of hoop stress. These results show that the sharp circumferential notch ($K_{t,n} = 4.5$) resulted in lower fatigue strengths than the un-notched case, whereas notches with $K_{t,n} < 2$ resulted in higher net fatigue strengths than the un-notched case. Higher net fatigue strengths mean that the notch was less damaging than a uniform reduction in wall thickness to the same depth. The blunt circumferential notch did not have a statistically significant effect relative to the un-notched case indicating no fatigue sensitivity to this notch type. Unlike the two notched uniaxial test sets, the difference in F_{an} for the two circular notches subject to bending loading was not statistically significant, showing the root radius did not have a significant effect in this case.

4.4. Fatigue model parameters from FEA

To provide readers with an understanding of the workings of the notch fatigue models, the model parameters calculated using the FEA results for each specimen type are listed in Table 2 and example results are shown in Figs. 12 and 13. The workings of the volume-based methods deserve particular attention due to their more complex nature than the point-based methods. As expected, a much larger volume of the un-notched specimens experienced the highest stress amplitudes compared to the notched specimens, although the maximum stress amplitudes experienced by the notched specimens was higher. The less

Fig. 12. FEA predicted Effective Volume weighting, $(\sigma_{a,SWT}/\sigma_{a,SWT,max})^{M_{ES}}$, for the sharp notch bending specimen under bending loading for the quarter-pipe model showing the weighting assigned to elements away from the notch. The axial direction is left-to-right, and the notch is located at the bottom left.

binary nature of the Effective Volume approach meant V_{eff} was usually larger than $V_{95\%}$. For example, for the sharp notch uniaxial specimen a volume of material nearly 10 times greater contributed to V_{eff} than $V_{95\%}$ (1.57 mm^3 compared to 0.21 mm^3). The very small $V_{95\%}$ values calculated in some cases is likely to be the reason that the HSV predictions from FEA did not converge for some test sets.

The Effective Volume approach showed some interesting behaviour in the way it weighted stresses in material volume near and far from the notch. For cases where the notch $K_{t,n}$ value was higher than 2 the Effective Volume approach only considered stresses occurring in the material proximate to the peak stress. For example, for the sharp notch uniaxial specimen, material volume with a $(\sigma_{a,SWT}/\sigma_{a,SWT,max})^{M_{ES}}$ weighting between 1 and 0.01 comprised over 90 % of V_{eff}. Volume with this weighting only extended to a depth of approximately 0.18 mm behind the notch root, but did occur the whole way around the specimen's circumference. On the other hand, for cases where the notch $K_{t,n}$ value was less than 2 the Effective Volume approach considered stresses in material a significant distance from the notch. For example, for the sharp circular notch under bending loading, material volume with a $(\sigma_{a,SWT}/\sigma_{a,SWT,max})^{M_{ES}}$ weighting between 10^{-3} and 10^{-4} comprised over 75 % of V_{eff}. Volume with this weighting extended from the notch along the specimen invert for around 70 mm in each direction, as shown by Fig. 12. Additionally, material with a weighting between 1 and 10^{-3} only comprised 1 % of V_{eff}, indicating the Effective Volume approach attributed minimal significance to the notch root stresses in this case. This shows how the Effective Volume approach varied the significance attributed to the local notch stresses and the gross stress state for different notch types. The behaviour was very different to the Highly Stressed Volume approach which only considered material volume at the notch root regardless of $K_{t,n}$ (compare Fig. 13c and 13d, for example).

4.5. Fatigue life estimates

The cycles-to-failure estimates used to test the effectiveness of the multiaxial notch fatigue criteria detailed in Section 2 are plotted in Fig. 14. The quantified prediction errors for each model are also given in Fig. 15 in terms of T_{RMS}, where smaller T_{RMS} values indicate better prediction accuracy. For each model, predictions were made for each fatigue data set not used to calibrate that model. It was not possible to make predictions for the un-notched bending and un-notched biaxial data sets using Heywood's relation due to the absence of a notch, and the

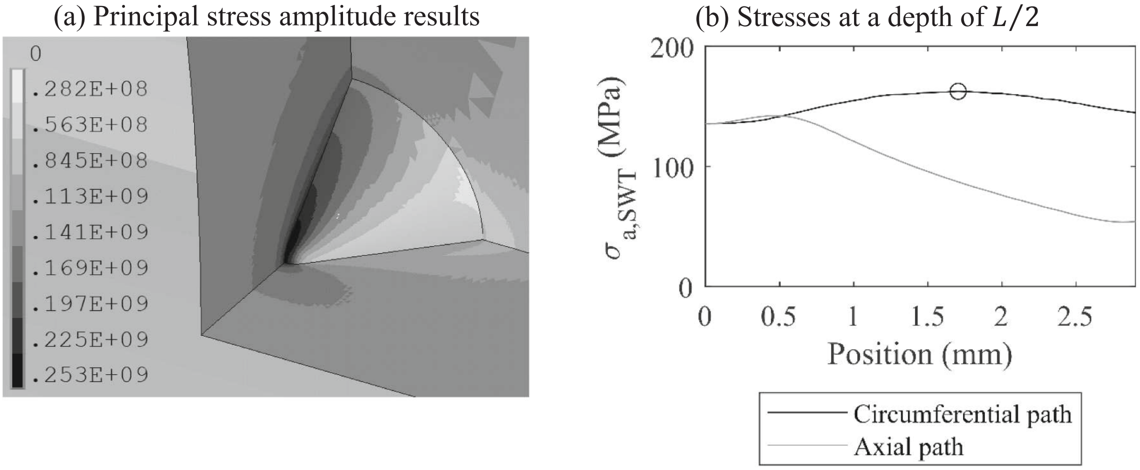
(a) Principal stress amplitude results

(b) Stresses at a depth of $L/2$

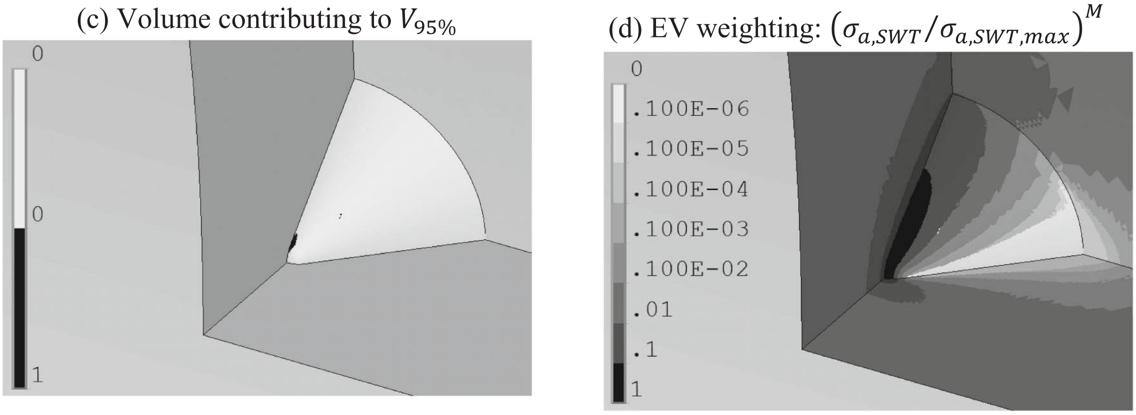
(c) Volume contributing to $V_{95\%}$

(d) EV weighting: $(\sigma_{a,SWT}/\sigma_{a,SWT,max})^M$

Fig. 13. FEA results for the sharp notch bending specimen subjected to an 8 kN amplitude bending load, illustrating how the key results used to make fatigue life predictions relate to the notch geometry. The axial direction in the sub-figures is left-to-right.

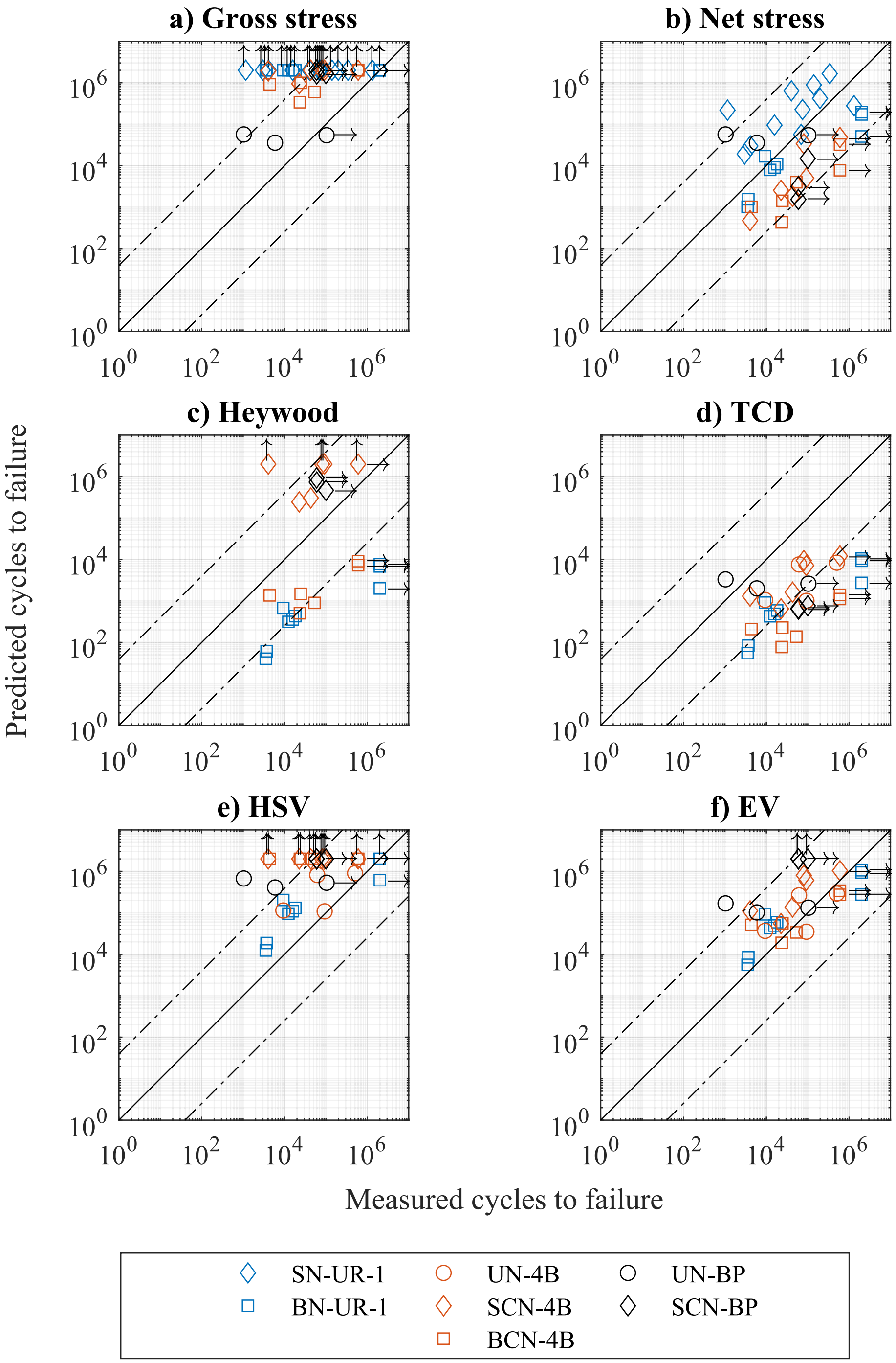

Fig. 14. Multiaxial notch fatigue model predictions compared against the experimentally determined cycles to failure. Each notch fatigue model was coupled with the Smith-Watson-Topper multiaxial fatigue criterion to make predictions. The chain lines show the scatter bands of the un-notched uniaxial data for reference.

un-notched bending data was used to calibrate the gross and net stress predictions. Predictions which exceeded 2×10^6 cycles are indicated with a vertical arrow on Fig. 14.

The gross stress approach consistently overestimated the fatigue lives of notched specimens showing that notches always reduced the fatigue strength of specimens. On the other hand, the net stress approach provided reasonable predictions for most data sets with only a small number of points falling outside of the scatter bands.

Heywood's equation provided conservative predictions for the blunt notch data sets. This indicates that when calibrated with relatively high $K_{t,n}$ data the model does not capture the behaviour of lower $K_{t,n}$ notches. The Theory of Critical Distances Point Method provided overly conservative predictions for most data sets. The Highly Stressed Volume approach tended towards non-conservative predictions for all data sets, except the blunt notch uniaxial and un-notched bending data.

The Effective Volume approach provided good predictions for all data sets, except the un-notched biaxial data set where one prediction fell outside the un-notched uniaxial $R = -1$ scatter bands on the non-conservative side. The Effective Volume received the best T_{RMS} prediction accuracy score for the three bending data sets and a lower T_{RMS} than the benchmark for the blunt notch uniaxial data set.

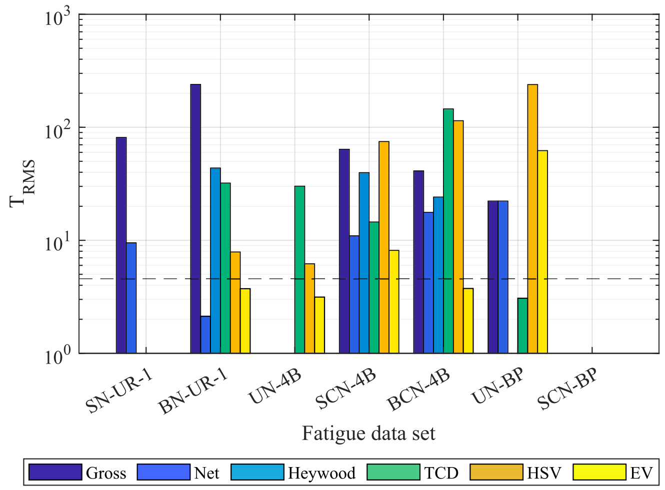

Fig. 15. Prediction error results for each notch fatigue model, enabling comparison of each models' relative performance for each fatigue data set. Smaller TRMS values indicate better prediction accuracy. As a benchmark, the dashed line shows the TRMS value for UN-UR-1 from [24] predicted using $\sigma_{1,a}$.

5. Discussion

This section looks across the experimental results to determine the fatigue sensitivity of GCI pipes to different load types and localised notches. Additionally, the numerical modelling results and notch fatigue model predictions are used to establish the suitability of the four models detailed in Section 2 to predict the fatigue life of pitted GCI pipes. This section ends with a review of the wider applicability of this work.

5.1. *The effect of bending and out-of-phase biaxial loading*

Bending loading had a statistically significant effect on the fatigue strength of the GCI specimens (see Table 4). The un-notched bending fatigue strength of the GCI pipe specimens was 1.43 times higher than the uniaxial fatigue strength of specimens tested under the same stress ratio (see Fig. 8), which falls within the 1.38 to 1.69 range reported by Heywood [18] for non-pipe GCI specimens. Despite bending loading resulting in higher fatigue strengths for the GCI specimens, 180° out-of-phase bending and internal pressure loading reduced the fatigue strength of specimens by a similar proportion to torsional loading. On average, the fatigue strengths of the un-notched torsion data from [24] and un-notched bending and internal pressure data (from a hoop-stress perspective) were 22 % and 28 % lower than the comparable uniaxial cases, respectively. These results support the idea that 180° out-of-phase biaxial loading, where the two principal stress components are of equal amplitude, is a particularly damaging load case for un-notched GCI. The effect of 180° out-of-phase biaxial loading on the fatigue life of GCI specimens can be explained by the additional crack opening due to the Poisson effect of the transverse stresses acting on the crack, which is likely to be why fatigue strength reduction caused by this loading is close to the material's 0.28 Poisson ratio. This effect is captured by the normal strain amplitude term of the SWT criterion (Eq. (1).

Unlike the un-notched specimens, 180° out-of-phase biaxial loading did not have a clear effect on the fatigue strength of the sharp circular notch specimens, relative to the same specimens exposed to only bending loading (see Fig. 11). However, the lack of failures in the sharp circular notch specimen biaxial loading data set makes such a comparison difficult. It is possible that the sharp circular pit specimens were less sensitive to biaxial loading than the un-notched specimens because the stress hot-spots due to bending loading and internal pressure loading occurred at different locations within the pit (note the highly local nature of the stress concentration caused by bending loading in Fig. 13a). Further investigation into the interaction between localised pits and biaxial loading would be beneficial to confirm whether 180° out-of-phase biaxial loading represents a more damaging load case for GCI pipes featuring localised corrosion pits.

5.2. *The effect of notches on fatigue strength*

The fatigue strength of pipe specimens was always reduced when a notch was introduced, relative to a specimen with no notch and the same gross dimensions, as illustrated by the poor gross stress fatigue life predictions (Fig. 14a). The reduction in fatigue strength caused by notches could partly be described by the reduction in wall thickness through considering the net stress state (see Figs. 11 and 14b). However, the sharp circumferential notch tested under uniaxial loading (characterised by $K_{t,n} = 4.5$) reduced the fatigue strength of the pipes tested, relative to an un-notched pipe subject to the same net stress, whereas notches with $K_{t,n} < 2$ resulted in higher fatigue strengths than the un-notched case (see Fig. 11). This shows that the magnitude of the stress concentration caused by a notch, and therefore a corrosion pit, can have a significant effect on the fatigue strength of GCI, despite the very low notch sensitivity of this material. $K_{t,n}$ is determined by the notch geometry, including root radius and plan shape, and the applied stress direction.

The net stress fatigue notch sensitivity of specimens with $K_{t,n} = 4.5$ ($q = 0.05$, calculated using F_{an}) was within the range reported by Lampman [17] and Taylor et al. [16] for non-pipe GCI specimens featuring sharp circumferential notches ($0.00 \leq q \leq 0.27$). However, fatigue tests of GCI specimens featuring localised, low $K_{t,n}$ notches have not previously been reported, so the very low fatigue notch sensitivity of GCI to this type of notches ($-1.93 \leq q \leq -0.30$) has not been observed.

5.3. *Estimating fatigue life*

5.3.1. *Net stress approach*

Predicting the fatigue life of notched pipes using the Smith-Watson-Topper criterion with the global net stress state and bending load fatigue effect factor ($K_b = 0.7$) provided reasonable predictions because of the material's relatively low notch sensitivity. The net stress predictions were best for un-notched specimens, or when $K_{t,n}$ was close to 2 (see Fig. 11). However, the net stress predictions fell outside the uniaxial scatter bands for relatively high or low $K_{t,n}$ corrosion pits, with errors exceeding two decades. As a result, some understanding of the corrosion pit shapes present in a particular pipeline or GCI component, and their corresponding $K_{t,n}$ values, is needed to determine whether the net stress can make usable fatigue life predictions.

5.3.2. *Effective Volume approach*

The coupled Effective Volume approach and Smith-Watson-Topper criterion provided the best notch fatigue predictions overall, except for the un-notched biaxial loading case. These good predictions were achieved because the Effective Volume approach was able to account for the bending load effect and distinguish between the effects of high and low $K_{t,n}$ notches by changing the significance attributed to local notch stresses and the gross stress state, as discussed above. The calibration constant M_{ES} is a function of the internal defect size distribution [22], so the calibrated value of 6.90 determined here is likely to be applicable to spun GCI pipes with similar microstructural properties to the BS 416–2 pipes tested here.

The underlying theory of the Effective Volume approach is based on the weakest-link concept. Specifically, exposing a larger volume of material to a higher or more damaging stress amplitude increases the probability of a larger defect (or “weaker link”) being exposed to that stress, reducing the fatigue strength of the specimen [21,22]. Paradoxically, for low $K_{t,n}$ notch cases (such as the sharp circular notch under bending loading) cracks did not occur in the large volume remote from the notch that was given a substantial weighting by the Effective Volume approach (this could be up to 70 mm from the notch), and instead always occurred at the notch (see Fig. 3d). This seems contrary to the idea that larger effective volumes correspond to a greater chance of finding a critical defect because crack initiations distributed across the whole critical volume would be expected. Literature applications of the Effective Volume approach are limited to axisymmetric cylindrical specimens [22], so this observation is unlikely to have been relevant before, but it is certainly relevant to the application of the approach to real components. The accurate notch fatigue predictions made by the Effective Volume approach for low $K_{t,n}$ localised notches therefore do not have a clear link to the physical notch fatigue process.

5.3.3. *Heywood's relation and the Theory of critical Distances point method*

This work has shown that the two notch fatigue approaches that have previously been applied to GCI are unsuitable for predicting the fatigue notch effect for pitted GCI water pipes. Heywood's equation coupled with the Smith-Watson-Topper criterion provided good predictions for high $K_{t,n}$ notches and poor predictions for low $K_{t,n}$ notches. Previous validation of Heywood's equation was limited to sharp circumferentially notched specimens [18], so this limitation had not been noted. Given the likely prevalence of low $K_{t,n}$ notches in GCI water pipes Heywood's equation can be considered unsuitable for this application.

The Theory of Critical Distances' predictions were mainly conservative which is likely because the remaining wall thickness behind the notch root (approximately 1.8 mm) was less than the range of L quoted for GCI in the literature (3.15 to 4.41 mm) [20]. This implies that the 0.87 mm value of L calculated was specific to the combination of wall thickness and notch root radius used for calibration. This agrees with the observation of Taylor [27] that the Theory of Critical Distances is not applicable to brittle materials where the specimen size approaches L as the assumption of local control breaks down and the specimen boundaries affect the notch tip processes. This limitation is relevant to GCI water pipes because many notch fatigue scenarios are likely to involve remaining wall thicknesses approaching, or less than, 3 mm considering the initial specified thickness of 3'' Class C spun-cast pipes was 7.4 mm [40]. The similarities between Heywood's equation and the TCD PM, in that they both use the stress at a point behind the notch root to make predictions, makes it likely that the poor predictions offered by Heywood's equation were also due to the low wall thickness of the specimens tested here.

5.3.4. *SN curve inflection point*

For the specimens tested that featured blunt notches (3.2 mm $\leq r \leq$ 5.5 mm) the inflection point of the fatigue curves, marking the transition from high-cycle fatigue to very high-cycle fatigue, appears to have occurred at shorter fatigue lives than the other notched and un-notched specimens (see Figs. 7 and 6). Specifically, this transition appears to have occurred at around 10^5 cycles for the blunt notch specimen and around 10^6 cycles for the other specimens. Chaves et al. [41] observed that early crack growth behaviour in metals at longer fatigue lives is heavily influenced by notch root radius, which may explain this behaviour.

Determining the exact position of the S-N curve inflection point, and the mechanisms that may cause its position to be influenced by notch root radius, was outside the scope of this work. However, the runout data obtained give a strong suggestion that some link exists between notch sharpness and the S-N curve inflection point. Further investigation of this link using the classic staircase testing method [37] would be beneficial. Until such an investigation is completed, a cautious approach to applying the net stress and Effective Volume models to long fatigue lives is recommended. Specifically, both models have the potential to make very conservative predictions for fatigue lives greater than 10^5 load cycles for certain large root radius notch geometries. This is because the notch fatigue models evaluated here are valid only for high-cycle fatigue and cannot predict this apparent change in fatigue cracking mode.

5.4. *Practical significance*

The combined EV and SWT criterion is the first validated model for predicting the fatigue strength of pitted GCI pipes subject to bending loading, or more generally, for predicting the fatigue strength of thin GCI components with stress raisers. The damaging effect of a particular corrosion pit loading condition can now be assessed for spun-cast GCI pipes which are similar to those tested in this work. This provides an essential tool that, when coupled with advanced in-pipe inspection techniques, will enable asset managers to make informed pipe-level replacement decisions to reduce leakage. To apply this approach, detailed pit shape measurements are required. However, if detailed corrosion pit measurements are not available but the pit depth is known, this work has shown that the SWT criterion applied directly to the net stress state can provide a reasonable estimate of a pipe's fatigue strength.

This work has also shown that longitudinal bending fatigue loads cause complete GCI pipe barrels to demonstrate fatigue strengths 43 % higher than loading which results in a uniform application of stress, whereas 180° out-of-phase bending and internal pressure loading reduces the fatigue strength of un-notched specimens by around 28 %. This raises the possibility that bending loads, while less damaging in isolation, may amplify the effect of internal pressure loads if they occur out-of-phase. It is important to note that the percentage changes in fatigue strength quoted above for bending and biaxial loading were determined from a relatively small number of tests using similar specimens. As a result, a larger testing programme including GCI pipes with a variety of mechanical and microstructural properties would be needed to confirm the general applicability of these load effects.

Beyond water pipe applications, this work has shown that the combined EV and SWT criterion can predict the high-cycle fatigue strength of a notched metallic component featuring non-metallic inclusions and voids. Furthermore, this criterion was shown to work with thin components where the TCD was found to return less effective life estimates. As a result, the EV approach, in combination with the SWT or another multiaxial fatigue criterion, should be considered for fatigue analysis of other thin, notched components. Potential applications include automotive and maritime components made from GCI [19,42], as well as components made from other metals containing non-metallic inclusions and voids such as ductile iron [43,44], sintered iron [45], and 3D-printed metals [46].

6. Conclusions

The work presented in this paper experimentally validates a model that can be used to assess the damaging effect of corrosion pitting on GCI pipes subject to bending and biaxial fatigue loading. The conclusions of this work are as follows:

- The high-cycle fatigue strength of pitted spun GCI water pipes subject to uniaxial and bending fatigue loading in laboratory conditions can be predicted using the combined Smith-Watson-Topper multiaxial fatigue criterion and Effective Volume notch fatigue model.
- When $2 \leq K_{t,n} \leq 4$ the Smith-Watson-Topper criterion can be applied directly to the net stress state to make fatigue life predictions, simplifying the analysis.
- 180° out-of-phase biaxial fatigue stresses can reduce the fatigue strength of GCI pipes featuring uniform wall-loss corrosion by up to 28 %.
- The magnitude of the stress concentration caused by a notch, and therefore a corrosion pit, can have a significant effect on the fatigue

strength of GCI water pipes, despite the very low notch sensitivity of this material.

- GCI pipes subject to longitudinal bending fatigue demonstrate fatigue strengths up to 43 % higher than uniaxial loading.
- The EV approach, in combination with the SWT or another multiaxial fatigue criterion, should be considered for fatigue analysis of other thin, notched components featuring inclusions or internal voids.

CRediT authorship contribution statement

E.D.A. John: Writing – original draft, Visualization, Validation, Investigation, Formal analysis, Data curation. **J.B. Boxall:** Writing – review & editing, Supervision, Funding acquisition, Conceptualization. **R.P. Collins:** Writing – review & editing, Supervision, Funding acquisition, Conceptualization. **E.T. Bowman:** Writing – review & editing, Supervision, Funding acquisition, Conceptualization. **L. Susmel:** Writing – review & editing, Supervision, Project administration, Methodology, Funding acquisition, Conceptualization.

Funding

This research was funded by UK Water Industry Research (UKWIR) and the Engineering and Physical Sciences Research Council (EPSRC) through the Water Infrastructure and Resilience (WIRe) Centre for Doctoral Training (EPSRC funding reference: EP/S023666/1).

Declaration of competing interest

The authors declare that they have no known competing financial interests or personal relationships that could have appeared to influence the work reported in this paper.

Acknowledgements

The authors would like to thank Dennis Dellow and Jeremy Heath from UKWIR for bringing an experienced industry perspective to the project. The authors give a special thanks to the University of Sheffield technicians Paul Blackbourn, Richard Kay, Martin Taylor, Mario Dorna, Sam Gibson, Kieran Nash, Kieren Howarth, and Paul Bentley for their invaluable work and assistance.

Data availability

Research data available at the following repository: https://doi.org/10.15131/shef.data.29183945

References

[1] J. Sanders, D. Marshallsay, G. Mountfort, G. Fox, M. Butler, A Leakage Routemap to 2050, 2022. https://www.water.org.uk/news-item/milestone-leakage-routemap-to-revolutionise-the-reduction-of-leakage-from-pipes/ (accessed June 15, 2022).

[2] Barton NA, Farewell TS, Hallett SH, Acland TF. Improving pipe failure predictions: Factors affecting pipe failure in drinking water networks. Water Res 2019;164:114926. https://doi.org/10.1016/j.watres.2019.114926.

[3] Folkman S. Water Main break rates In the USA and Canada: a Comprehensive Study. UT: Logan; 2018. https://digitalcommons.usu.edu/ (accessed February 28, 2024).

[4] R. Logan, M.J. Mulheron, D.A. Jesson, P.A. Smith, T.S. Evans, N. Clay-Michael, J.T. Whiter, Graphitic corrosion of a cast iron trunk main: Implications for asset management, in: WIT Transactions on The Built Environment, Vol 139, WIT Press, 2014. 10.2495/UW140351.

[5] Yamamoto K, Mizoguti S, Yoshimitsu K, Kawasaki J. Relation between graphitic corrosion and strength degradation of cast iron pipe. Boshoku Gijutsu 1983;32:157–62. https://doi.org/10.3323/jcorr1974.32.3_157.

[6] Seica MV, Packer JA. Mechanical Properties and Strength of Aged cast Iron Water Pipes. J Mater Civ Eng 2004;16:69–77. https://doi.org/10.1061/(asce)0899-1561(2004)16:1(69).

[7] Zhang C, Rathnayaka S, Shannon B, Ji J, Kodikara J. Numerical interpretation of pressurized corroded cast iron pipe tests. Int J Mech Sci 2017;128:116–24. https://doi.org/10.1016/j.ijmecsci.2017.04.015.

[8] Atkinson K, Whiter JT, Smith PA, Mulheron M. Failure of small diameter cast iron pipes. Urban Water 2002;4:263–71. https://doi.org/10.1016/S1462-0758(02)00004-3.

[9] P. Marshall, Understanding burst rate patterns of water pipes, 01/WM/02/16 (2001). https://ukwir.org/ (accessed December 2, 2024).

[10] Randeniya C, Robert DJ, Li CQ, Kodikara J. Large-scale experimental evaluation of soil saturation effect on behaviour of buried pipes under operational loads. Can Geotech J 2020;57:205–20. https://doi.org/10.1139/cgj-2018-0544.

[11] Jara-Arriagada C, Stoianov I. High resolution water pressure monitoring for the assessment of fatigue damage in water pipes. In: in: 2nd International Joint Conference on Water Distribution Systems Analysis and Control in the Water Industry; 2022. https://doi.org/10.4995/WDSA-CCWI2022.2022.14813.

[12] Rathnayaka S, Shannon B, Rajeev P, Kodikara J. Monitoring of pressure transients in water supply networks. Water Resour Manag 2016;30:471–85. https://doi.org/10.1007/s11269-015-1172-y.

[13] Brevis W, Susmel L, Boxall J. Investigating in-service failures of water pipes from a multiaxial notch fatigue point of view: a conceptual study. Proc Inst Mech Eng C J Mech Eng Sci 2015;229. https://doi.org/10.1177/0954406214553020.

[14] Jiang R, Rathnayaka S, Shannon B, Zhao X-L, Ji J, Kodikara J. Analysis of failure initiation in corroded cast iron pipes under cyclic loading due to formation of through-wall cracks. Eng Fail Anal 2019;103:238–48. https://doi.org/10.1016/j.engfailanal.2019.04.031.

[15] Pilkey WD, Pilkey DF. Peterson's stress concentration factors. 3rd ed. Hoboken, New Jersey, US: John Wiley & Sons Inc; 2008.

[16] Taylor D, Hughes M, Allen D. Notch fatigue behaviour in cast irons explained using a fracture mechanics approach. Int J Fatigue 1996;18:439–45. https://doi.org/10.1016/0142-1123(96)00018-7.

[17] Lampman. S, Fatigue and Fracture Properties of Cast Irons, in: ASM Handbook, Vol. 19: Fatigue and Fracture, 1996: pp. 665–679. https://doi-org.sheffield.idm.oclc.org/10.31399/asm.hb.v19.a0002399.

[18] Heywood RB. Designing against Fatigue, first. London: Chapman and Hall Ltd.; 1962.

[19] Taylor D. Analysis of fatigue failures in components using the theory of critical distances. Eng Fail Anal 2005;12:906–14. https://doi.org/10.1016/j.engfailanal.2004.12.007.

[20] Susmel L. The theory of critical distances: a review of its applications in fatigue. Eng Fract Mech 2008;75:1706–24. https://doi.org/10.1016/j.engfracmech.2006.12.004.

[21] Kuguel R. A relation between theoretical stress concentration factor and fatigue notch factor deduced from the concept of highly stressed volume. ASTM Proceedings 1961;61:732–48.

[22] Bomas H, Linkewitz T, Mayr P. Application of a weakest-link concept to the fatigue limit of the bearing steel SAE 52100 in a bainitic condition. Fatigue Fract Eng Mater Struct 1999;22:733–41. https://doi.org/10.1046/j.1460-2695.1999.t01-1-00211.x.

[23] J. Fash, D.F. Socie, Fatigue behaviour and mean effects in grey cast iron, Int J Fatigue July (1982) 137–142. 10.1016/0142-1123(82)90040-8.

[24] John E, Boxall J, Collins R, Bowman E, Susmel L. Multiaxial fatigue of water pipe grey cast iron. Int J Fatigue 2024;178:108002. https://doi.org/10.1016/j.ijfatigue.2023.108002.

[25] Smith P, K.N., Topper, T.H., Watson,. A stress–strain function for the fatigue of metals. J Mater 5 1970:767–78. https://www.researchgate.net/publication/269929853_14_Smith_K_N_Watson_P_and_Topper_T_H_'A_StressStrain_Function_for_the_Fatigue_of_Metals_nl_of_Marls_1MLSA_5_4_767-778_Dee_1070.

[26] Dowling NE, Calhoun CA, Arcari A. Mean stress effects in stress-life fatigue and the Walker equation. Fatigue Fract Eng Mater Struct 2008;32:163–79. https://doi.org/10.1111/j.1460-2695.2008.01322.x.

[27] Taylor D. The Theory of critical Distances: a New Perspective in Fracture Mechanics, first. Oxford: Elsevier Science & Technology; 2007. https://ebookcentral.proquest.com/lib/sheffield/detail.action?docID=330158. (accessed January 13, 2023.

[28] Al Zamzami I, Susmel L. On the accuracy of nominal, structural, and local stress based approaches in designing aluminium welded joints against fatigue. Int J Fatigue 101 2017:137–58. https://doi.org/10.1016/j.ijfatigue.2016.11.002.

[29] Louks R, Gerin B, Draper J, Askes H, Susmel L. On the multiaxial fatigue assessment of complex three-dimensional stress concentrators. Int J Fatigue 2014;63:12–24. https://doi.org/10.1016/j.ijfatigue.2014.01.001.

[30] Van Hooreweder B, Moens D, Boonen R, Sas P. Fatigue strength analysis of notched aluminium specimens using the highly stressed volume method. Fatigue Fract Eng Mater Struct 2012;35:154–9. https://doi.org/10.1111/j.1460-2695.2011.01602.x.

[31] Ai Y, Zhu SP, Liao D, Correia JAFO, De Jesus AMP, Keshtegar B. Probabilistic modelling of notch fatigue and size effect of components using highly stressed volume approach. Int J Fatigue 2019;127:110–9. https://doi.org/10.1016/j.ijfatigue.2019.06.002.

[32] Tomaszewski T, Strzelecki P, Mazurkiewicz A, Musial J. Probabilistic estimation of fatigue strength for axial and bending loading in high-cycle fatigue. Materials 2020;13. https://doi.org/10.3390/ma13051148.

[33] British Standards Institution. Discharge and ventilating pipes and fittings, sand-cast or spun in cast iron - Part 2: specifications for socketless systems. BS 1990;416–2:1990. https://bsol-bsigroup-com.sheffield.idm.oclc.org/Bibliographic/BibliographicInfoData/000000000000225830.

[34] John E, Boxall J, Collins R, Bowman E, Susmel L. Fatigue failure analysis of grey cast iron water pipes accounting for fatigue strength variation. Eng Fail Anal 2024;165:108762. https://doi.org/10.1016/j.engfailanal.2024.108762.

[35] John EDA, Boxall JB, Collins RP, Bowman ET, Susmel L. An Experimental Method for Fatigue Testing cast Iron Water Pipes using combined Internal Water pressure

and Bending Loads. Exp Mech 2025. https://doi.org/10.1007/s11340-025-01153-6.

[36] Fatigue Data ASTM E739–10 2015. https://doi.org/10.1520/E0739-10R15.

[37] Compass 1963. https://doi.org/10.1520/STP91A-EB.

[38] Dekking F, Kraaikamp C, Lopuhaa H, Meester L. Confidence intervals for the mean. In: A Modern Introduction to Probability and Statistics: Understanding Why and How. London Limited: Springer-Verlag; 2005. p. 341–60.

[39] Walat K, Łagoda T. Lifetime of semi-ductile materials through the critical plane approach. Int J Fatigue 2014;67:73–7. https://doi.org/10.1016/j.ijfatigue.2013.11.019.

[40] British Standards Institution. Centrifugally cast (spun) iron pressure pipes for water, gas & sewage. accessed December 9, 2024 BS 1958;1211:1958. https://bsol.bsigroup.com/.

[41] Chaves V, Madrigal C, Navarro A. Non-propagating cracks in notched components at the fatigue limit analysed with a microstructural model. Theor Appl Fract Mech 2018;95:119–26. https://doi.org/10.1016/j.tafmec.2018.02.008.

[42] Gigan G, Norman V, Ahlström J, Vernersson T. Thermomechanical fatigue of grey cast iron brake discs for heavy vehicles. Proc IMechE Part D: J Automobile Engineering 2019;233(2):453–67. https://doi.org/10.1177/0954407017739723.

[43] Berto F, Lazzarin P, Tovo R. Multiaxial fatigue strength of severely notched cast iron specimens. Int J Fatigue 2014;67:15–27. https://doi.org/10.1016/j.ijfatigue.2014.01.013.

[44] Pedranz M, Fontanari V, Raghavendra S, Santus C, Zanini F, Carmignato S, et al. A new energy based highly stressed volume concept to investigate the notch-pores interaction in thick-walled ductile cast iron subjected to uniaxial fatigue. Int J Fatigue 2023;169:107491. https://doi.org/10.1016/j.ijfatigue.2022.107491.

[45] Zhu S-P, Yu Z-Y, Correia J, De Jesus A, Berto F. Evaluation and comparison of critical plane criteria for multiaxial fatigue analysis of ductile and brittle materials. Int J Fatigue 2018;112:279–88. https://doi.org/10.1016/j.ijfatigue.2018.03.028.

[46] Razavi N, Askes H, Berto F, Susmel L. Length scale parameters to estimate fatigue lifetime of 3D-printed titanium alloy Ti6Al4V containing notches in the as-manufactured condition. Int J Fatigue 2023;167:107348. https://doi.org/10.1016/j.ijfatigue.2022.107348.